

# Effective model and pairing tendency in bilayer Ni-based superconductor $\text{La}_3\text{Ni}_2\text{O}_7$

Yuhao Gu,<sup>1,\*</sup> Congcong Le,<sup>2,\*</sup> Zhesen Yang,<sup>1</sup> Xianxin Wu,<sup>3,†</sup> and Jiangping Hu<sup>1,4,‡</sup>

<sup>1</sup>Beijing National Laboratory for Condensed Matter Physics and Institute of Physics, Chinese Academy of Sciences, Beijing 100190, China

<sup>2</sup>RIKEN Interdisciplinary Theoretical and Mathematical Sciences (iTHEMS), Wako, Saitama 351-0198, Japan

<sup>3</sup>CAS Key Laboratory of Theoretical Physics, Institute of Theoretical Physics, Chinese Academy of Sciences, Beijing 100190, China

<sup>4</sup>Kavli Institute for Theoretical Sciences, University of Chinese Academy of Sciences, Beijing 100190, China

Since the discovery of cuprate, the origin of high- $T_c$  superconductivity has been an outstanding puzzle. Recently, high- $T_c$  superconductivity was observed in a bilayer nickelate  $\text{La}_3\text{Ni}_2\text{O}_7$  under pressure, whose structure hosts the apical oxygen between two layers, distinct from multi-layer cuprates. Motivated by this discovery, we investigate its electronic structure using first-principle calculations and superconductivity instabilities from both weak-coupling and strong-coupling perspective. Based on the first-principle band structures, we construct a bilayer two-orbital model on a square lattice, which accurately captures the low-energy electronic properties. Within this model, we study pairing instability using both functional renormalization group approach and multi-orbital t-J model. An  $s_{\pm}$ -wave pairing with sign-reversal gaps on different Fermi surfaces is revealed, reminiscent of iron based superconductors. We also discuss the effect of orthorhombic distortion and three-dimensional electronic structures and possible experimental implications as well. Our study provides valuable insights into unique nature of electronic structure and superconductivity in  $\text{La}_3\text{Ni}_2\text{O}_7$  and contributes to the understanding of unconventional superconductors.

Since the landmark discovery of high- $T_c$  superconductivity in cuprates[1], extensive research efforts have been dedicated to experimentally exploring noncopper-based compounds with similar crystal and electronic structure and theoretically elucidating the underlying mechanism [2–6]. The  $d^9$  configuration of  $\text{Cu}^{2+}$  in an octahedral crystal field is believed to be pivotal and the corresponding electronic structure can usually be described by the one-band Hubbard model. Owing to nickel being the neighbor of copper in the periodic table and  $\text{Ni}^{1+}$  hosting the same  $d^9$  electron count as  $\text{Cu}^{2+}$ , nickelates were identified as novel candidates for achieving high  $T_c$  superconductivity. Despite tremendous efforts in nickelates, superconductivity has only been realized until very recently in so-called “infinite-layer” nickelates  $(\text{Sr},\text{Nd})\text{NiO}_2$  thin films on a substrate [7–11]. Interestingly, superconductivity emerges around 5-15 K without a magnetic order. Similar to  $d^9$  cuprates, the low-energy states are dominated by the Ni  $d_{x^2-y^2}$  orbital but the contribution of Nd  $d$  orbitals introduce a self-doping in the Ni  $d_{x^2-y^2}$  orbital [12–15]. The  $T_c$  of the “infinite-layer” nickelates can be enhanced to be over 30 K with external pressure [10]. Still, their maximum  $T_c$  values have consistently fallen below the widely recognized McMillan limit.

Very recently, superconductivity was observed in the bilayer perovskite bulk nickelate  $\text{La}_3\text{Ni}_2\text{O}_7$  with a high transition temperature of  $T_c = 80$  K under high-pressure conditions [16]. With increasing pressure, the system experiences a structural transition from the Amam phase to the more symmetric Fmmm phase. Superconductivity appears in the latter phase for a pressure larger than 14 GPa. In sharp contrast to cuprates, the nominal valence here is  $d^{7.5}$  in  $\text{Ni}^{2.5+}$  and the apical oxygens between layers are preserved. Near

the Fermi level, the electronic structures are dominantly contributed by Ni  $d_{x^2-y^2}$  and  $d_{z^2}$  orbitals. The strong  $\sigma$  bonding in  $d_{z^2}$  orbitals between two layers is suggested to be crucial for superconductivity [16]. Therefore, the observation of high- $T_c$  superconductivity in the  $\text{La}_3\text{Ni}_2\text{O}_7$  challenges the understanding of high- $T_c$  cuprate. This reignites longstanding questions in the field of unconventional superconductivity, particularly in relation to the cuprates and related materials [4, 6]: (i) Whether  $d^9$  configuration plays a vital role in high- $T_c$  superconductivity; (ii) The absence of observed magnetism in  $\text{La}_3\text{Ni}_2\text{O}_7$  prompts the investigation of whether long-range antiferromagnetism is a key component in high- $T_c$  superconductivity; (iii) How does the  $d_{z^2}$  orbital influence high- $T_c$  superconductivity.

To help address these questions, we have studied the electronic structures of  $\text{La}_3\text{Ni}_2\text{O}_7$  through density functional theory (DFT) calculations and explored its superconductivity from repulsive interactions adopting both weak-coupling and strong-coupling approaches. Based on the first-principle band structures, we construct a bilayer two-orbital model on a square lattice, which captures the essential low-energy electronic structures. Neglecting the high-energy  $d_{z^2}$  antibonding state, we obtain a half-filled three-band model. Within the four-band model, we study pairing instability using both functional renormalization group (FRG) approach and multi-orbital t-J model. An  $s_{\pm}$ -wave pairing with sign-reversal gaps on different Fermi surfaces is revealed, analogous to iron based superconductors[17, 18]. The effect of orthorhombic distortion and three-dimensionality of electronic structures is discussed, together with possible experimental implications.

*Electronic structures*. We start with the crystal and electronic structures of  $\text{La}_3\text{Ni}_2\text{O}_7$ . The high-pressure phase of  $\text{La}_3\text{Ni}_2\text{O}_7$  in Fig.1(a), a bilayer Ni-based superconductor, exhibits a structural arrangement characterized by the presence of  $\text{NiO}_2$  bilayers, which are effectively separated by  $\text{LaO}$  layers. This intriguing configuration stems from the coordinated arrangement of two  $\text{NiO}_6$  octahedra, featuring the sharing of apical oxygen atoms, as visually represented in Fig.1(b).

\*These authors equally contributed to the work.

†Electronic address: xxwu@itp.ac.cn

‡Electronic address: jphu@iphy.ac.cn

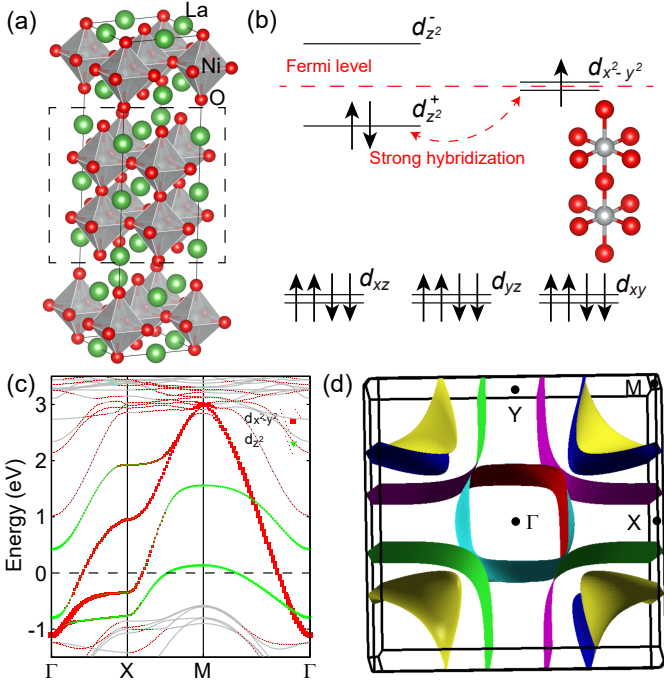


FIG. 1: (color online) (a) The crystal structure of  $\text{La}_3\text{Ni}_2\text{O}_7$  in the high-pressure phase. (b) The illustration of the two vertex-sharing  $\text{NiO}_6$  octahedra complex, the corresponding energy splitting of  $d$  orbitals, and the  $d$ -orbital filling configuration of two  $\text{Ni}^{2.5+}$ . (c) and (d) The DFT band structure and fermi surface in the primitive cell. The orbital characters near fermi level are represented by different colors, and the blue lines label the band structure from effective model.

Remarkably, these apical-oxygen-sharing  $\text{NiO}_6$  octahedra possess the capability to form an  $\text{NiO}_2$  bilayer, exhibiting an approximately square lattice structure. Here, the apical oxygen between the layers is in contrast to multi-layer cuprates. The  $e_g$  and  $t_{2g}$  orbitals are well separated in energy by octahedral crystal field, as demonstrated in Fig.1(b). Furthermore, the formation of bonding and antibonding in the  $d_{z^2}$  orbitals between two layer is evident from the analysis of orbital orientation. Considering the chemical valence of Ni atoms in  $\text{La}_3\text{Ni}_2\text{O}_7$  as  $\text{Ni}^{2.5+}$ , the corresponding  $d$ -orbital configuration is  $d^{7.5}$ , and thus the Fermi level is expected to reside between the bonding and antibonding states, as shown in Fig.1(b).

Fig.1(c) displays the band structure along high-symmetry paths in the primitive cell, in agreement with Ref.[19]. Consistent with the analysis of crystal field splitting, near the fermi level, the valence and conduction bands are predominantly attributed to  $d_{x^2-y^2}$  orbital, bonding state  $d_{z^2}^+$  and antibonding state  $d_{z^2}^-$ . Moreover, the band structure reveals the presence of both electron-like and hole-like Fermi surfaces in the primitive Brillouin zone. An electron-like pocket is located around the  $\Gamma$  point, whereas two hole pockets manifest around the  $M$  point, as shown in Fig.1(d). Notably, the two hole pockets primarily originate from the bonding state  $d_{z^2}^+$  and the  $d_{x^2-y^2}$  orbital, respectively. While, the electron-like

pocket is attributed to the strong mixture of  $d_{z^2}$  and  $d_{x^2-y^2}$  orbitals. From the Fermi surfaces, we deduce that the system is relatively two-dimensional and orthorhombic distortion has negligible effect on the electronic structures. Except enhanced band width and energy splitting between  $d_{z^2}^+$  and  $d_{z^2}^-$  in the high-pressure phase, the difference in electronic structures between the ambient-pressure and high-pressure phases is not significant (see supplementary material (SM)).

*Bilayer two-orbital model.* Based on the aforementioned analysis, we find the  $d_{x^2-y^2}$  and  $d_{z^2}$  orbitals play a prominent role near the Fermi level, while the deviation from the tetragonal lattice due to distortion remains relatively weak. Consequently, a bilayer two-orbital model on a square lattice, as depicted in Fig.2 (a), can be employed to effectively describe the low-energy electronic structure of  $\text{La}_3\text{Ni}_2\text{O}_7$  at high pressure. We introduce the operator  $\psi_{\mathbf{k}\sigma}^\dagger = [c_{tx^2\sigma}^\dagger(\mathbf{k}), c_{tz^2\sigma}^\dagger(\mathbf{k}), c_{bx^2\sigma}^\dagger(\mathbf{k}), c_{bz^2\sigma}^\dagger(\mathbf{k})]$ , where  $c_{\eta\alpha\sigma}^\dagger(\mathbf{k})$  represents the Fermionic creation operator with  $\eta, \alpha$  and  $\sigma$  being the layer, orbital and spin indices, respectively. The layer index  $\eta = t, b$  denotes the top and bottom layer and the orbital index  $\alpha = 1, 2$  represents the Ni  $d_{x^2-y^2}$  for 1 and the Ni  $d_{z^2}$  for 2. The tight-binding (TB) Hamiltonian can be written as

$$\mathcal{H}_{\text{TB}} = \sum_{\mathbf{k}\sigma} \psi_{\mathbf{k}\sigma}^\dagger [h(\mathbf{k}) - \mu] \psi_{\mathbf{k}\sigma}. \quad (1)$$

The corresponding matrix elements of  $h(\mathbf{k})$  and hopping parameters derived from a downfolding of the DFT bands onto four localized Wannier functions are given in the SM. With those parameters, the obtained band fits are provided in SM and both band dispersion and orbital characters (Fig.2(b)) reach a good agreement between DFT and the TB results. Along the  $\Gamma - X$  path,  $d_{x^2-y^2}$  and  $d_{z^2}$  orbital exhibit prominent hybridization due to the strong inter-orbital hopping between the nearest-neighbor sites. Along the  $\Gamma - M$  path, the  $d_{x^2-y^2}$  bands are almost degenerate due to its decoupling from the  $d_{z^2}$  orbitals and partial cancellation between inter-layer couplings. The strong orbital mixture near the Fermi level is in sharp contrast to the bilayer cuprates and infinite nickelates [20]. By neglecting the  $d_{z^2}$  anti-bond state, we can obtain a half-filled three-band model (details in SM).

Fig.2(c) displays the Fermi surfaces with a filling of three electrons. The electron-like pocket  $\alpha$  around the  $\Gamma$  point is attributed to an almost equal mixture between  $d_{x^2-y^2}$  and  $d_{z^2}$  orbitals. Meanwhile, the two hole-like pockets  $\beta$  and  $\gamma$  are dominantly contributed by  $d_{x^2-y^2}$  and  $d_{z^2}$  orbitals, respectively. The large  $d_{x^2-y^2}$  pocket  $\beta$  is just the representative Fermi surface of cuprates, except for some moderate hybridization with the  $d_{z^2}$  orbital along  $M - X$ . The pocket  $\gamma$ , originating from the inter-layer  $d_{z^2}$  bonding state, carries large density of states owing to the relative flat band dispersion around the  $M$  point. To characterize the Fermi surface nesting, we calculate the bare spin susceptibility and the largest eigenvalues of the susceptibility matrix  $\chi_0(\mathbf{q})$  are shown in Fig.2(d). The peak around the  $\mathbf{q}_3 = (\pi/2, \pi/2)$  vector is attributed to the Fermi surface nesting between electron-like  $\alpha$  and hole-like  $\gamma$  pockets. The peaks around the  $\mathbf{q}_1 = (0.47\pi, 0)$  and  $\mathbf{q}_2 = (\pi, 0)$  vectors are derived from the Fermi

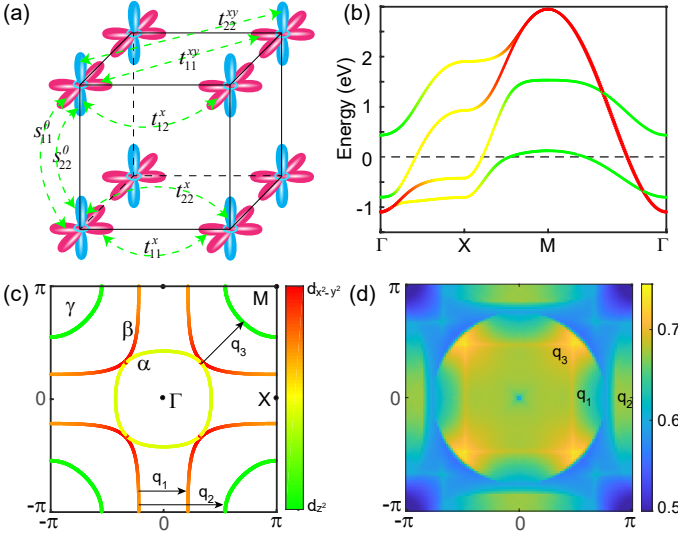


FIG. 2: (color online). (a) The schematic of main hopping parameters in the bilayer two-orbital model. Orbital-resolved band structure (b) and Fermi surfaces (c) from the tight-binding model with a electron filling  $n = 3$ . The orbital contributions are represented using different colors:  $d_{x^2-y^2}$  (red) and  $d_{z^2}$  (green). (d) Maximum eigenvalues of the susceptibility matrix  $\chi_0(\mathbf{q})$  in the 2D Brillouin zone.

surface nesting between  $\beta$  and  $\gamma$  pockets, as shown in Fig. 2 (d). Owing to the distinct shapes of the  $\alpha$  and  $\gamma$  pockets, the nesting at  $\mathbf{q} = (\pi, \pi)$  between them is not strong but can be enhanced by hole doping.

**FRG analysis.** To investigate the pairing symmetry and other correlated electronic states in  $\text{La}_3\text{Ni}_2\text{O}_7$ , we first consider the weak-coupling to intermediate-coupling limit and adopt the FRG approach, which treats all particle-hole and particle-particle channels on equal footing. This approach has widely used in the study of correlated electrons [21, 22].

In our FRG calculations, we consider the on-site Hubbard intra- and inter-orbital repulsion, Hund's coupling, as well as pairing hopping interactions,

$$\begin{aligned}
 H_{\text{int}} = & U \sum_{i\alpha} n_{i\alpha\uparrow} n_{i\alpha\downarrow} + U' \sum_{i,\alpha<\beta} n_{i\alpha} n_{i\beta} \\
 & + J \sum_{i,\alpha<\beta,\sigma\sigma'} c_{i\alpha\sigma}^\dagger c_{i\beta\sigma'}^\dagger c_{i\alpha\sigma'} c_{i\beta\sigma} \\
 & + J' \sum_{i,\alpha\neq\beta} c_{i\alpha\uparrow}^\dagger c_{i\alpha\downarrow}^\dagger c_{i\beta\downarrow} c_{i\beta\uparrow} \quad (2)
 \end{aligned}$$

where  $n_{i\alpha} = n_{\alpha\uparrow} + n_{\alpha\downarrow}$ .  $U, U', J$  and  $J'$  represent the onsite intra- and inter-orbital repulsion and the onsite Hund's coupling and pair-hopping terms for the Ni site, respectively. We use the Kanamori relations  $U = U' + 2J$  and  $J = J'$ . Within FRG formalism, we focus on the evolution of effective vertex function  $\Gamma^\Lambda(\mathbf{k}_1, \mathbf{k}_2, \mathbf{k}_3)$  as a function of an energy scale by progressively integrating out high-energy modes. The vertex function can be decoupled into the summation of bilinear terms  $\sum_{\xi, \mathbf{k}_1, \mathbf{k}_2} \Phi^{\Lambda, \xi}(\mathbf{k}_1, \mathbf{k}_2) \mathcal{O}_{\mathbf{k}_1}^{\xi, \dagger}(\mathbf{Q}) \mathcal{O}_{\mathbf{k}_2}^{\xi}(\mathbf{Q})$ , where  $\mathcal{O}_{\mathbf{k}}^{\xi}(\mathbf{Q})$  is the favored order operator in the particle-hole or particle-particle channels and  $\Phi^{\Lambda, \xi}$  is the corresponding  $\xi$ -channel

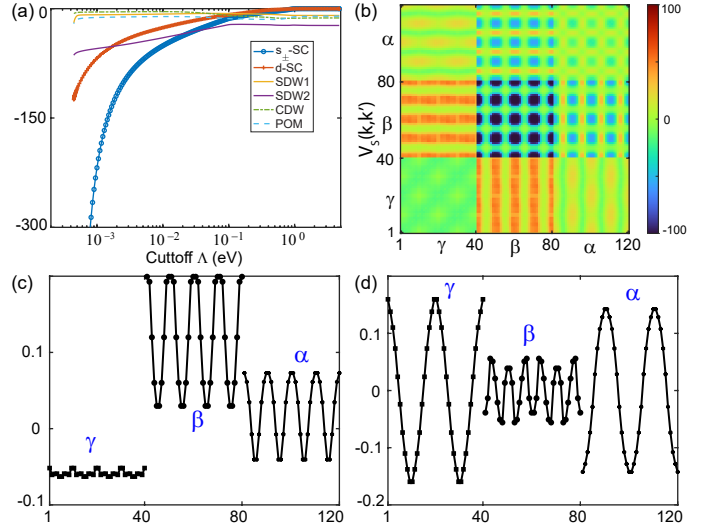


FIG. 3: (color online). (a) Typical flow of leading instabilities in both particle-hole and particle-particle channels at  $n = 3.0$ . SDW2 and SDW3 denote SDW states with the vector of  $\mathbf{q}_2$  and  $\mathbf{q}_3$ , respectively. (b) Cooper pairing scattering interactions on Fermi surfaces at the critical  $\Lambda_c$ . Gap functions of  $s_{\pm}$ -wave pairing (c) and  $d_{x^2-y^2}$ -wave pairing (d). The numbers 1-40, 41-80 and 81-120 represent patches on the  $\gamma$ ,  $\beta$  and  $\alpha$  pockets, respectively. Numbers increase in the anticlockwise direction, starting from the x-axis on each pocket (detailed numbering is in SM).

coupling. This channel coupling be further decoupled into  $\Phi^{\Lambda, \xi}(\mathbf{k}_1, \mathbf{k}_2) = \sum_m \phi_m^{\xi}(\Lambda) f_m^{\xi}(\mathbf{k}_1) f_m^{\xi}(\mathbf{k}_2)$ , where  $\phi_m^{\xi}(\Lambda)$  is an eigenvalue and  $f_m^{\xi}(\mathbf{k})$  is the corresponding eigenmode, transforming as an irreducible representation of the symmetry group of  $\Phi^{\Lambda, \xi}(\mathbf{k}_1, \mathbf{k}_2)$ . Approaching a critical energy scale  $\Lambda_c$ ,  $\Gamma^\Lambda(\mathbf{k}_1, \mathbf{k}_2, \mathbf{k}_3)$  tends to diverge and this signals an ordering tendency in the  $\xi$  channel with the most divergent  $\phi_m^{\xi}(\Lambda)$ .

Fig. 3(a) displays the representative FRG flow with a decreasing energy scale  $\Lambda$ . Away from the Fermi level, the spin density wave (SDW) fluctuation with a vector  $\mathbf{q}_2$  is established. With a decreasing cutoff  $\Lambda$ , the eigenvalues of two superconducting states grow rapidly, exceed the SDW state and finally diverge approaching to the Fermi level. This clearly suggests a spin-fluctuation-mediated pairing. At the critical  $\Lambda_c$ , the effective Cooper pairing scattering interaction  $V_S(\mathbf{k}, \mathbf{k}')$  in the spin-singlet channel is shown in Fig. 3(b). We find that the dominant inter-pocket Cooper pairing scattering occurs between the  $\beta$  and  $\gamma$  pockets and is repulsive, which predominantly determines the pairing symmetry. The dominant pairing state is  $s_{\pm}$ -wave and its gap function is shown in Fig. 3(c), where the gaps on the  $\beta$  pocket are anisotropic and the gaps of the  $\beta$  and  $\gamma$  have the opposite signs. The gap of the  $\alpha$  pocket exhibits a sign change owing to the sign-changing Cooper pairing scattering interaction between the  $\alpha$  and  $\beta$  pockets in the momentum space. The subdominant pairing is  $d_{x^2-y^2}$ -wave with SC nodes along the diagonal direction, as shown in Fig. 3(d). The segments from the  $\beta$  and  $\gamma$  pockets connected by the nesting vector  $\mathbf{q}_1$  still have the opposite superconducting gaps. With a large onsite Coulomb repulsion, our FRG calculations show that the SDW state with a vector

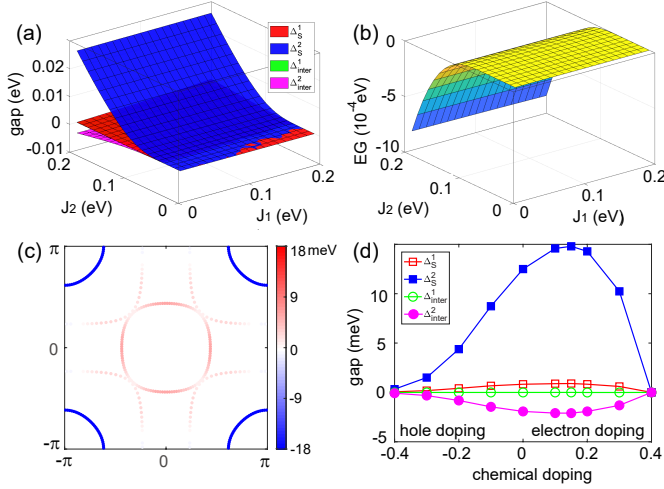


FIG. 4: (color online). (a) Leading superconducting gaps in different channels as a function of exchange couplings  $J_1$  and  $J_2$ . (b) Energy difference between the superconducting and normal states as a function of exchange parameters. (c) Superconducting gaps on the Fermi surfaces and (d) superconducting gaps as a function of charge doping, where  $J_1 = J_2 = 0.15$  is adopted. In the calculations, inter-layer exchange couplings  $J'_1 = J_1/5$  and  $J'_2 = J_2/2$  are used and varying the ratios will not qualitatively change the results.

$\mathbf{q}_1$  will be favored. We further study the external doping with a rigid band shift approximation and find the electron doping can enhance  $T_c$  without changing the pairing symmetry.

*Pairing in the t-J model.* In analogous to cuprates, we also investigate the pairing symmetry of  $\text{La}_3\text{Ni}_2\text{O}_7$  from a strong-coupling perspective. We adopt the two-orbital t-J model to investigate pairing symmetries for nickelates similar to iron-based superconductors [23, 24] and consider both the in-plane and out-of-plane antiferromagnetic couplings between the spin of Ni  $d_{x^2-y^2}/d_{z^2}$  orbitals,

$$H_J = \sum_{\langle ij \rangle \alpha} J_{ij}^\alpha (\mathbf{S}_{i\alpha} \mathbf{S}_{j\alpha} - \frac{1}{4} n_{i\alpha} n_{j\alpha}) \quad (3)$$

where  $\mathbf{S}_{i\alpha} = \frac{1}{2} c_{i\alpha\sigma}^\dagger \boldsymbol{\sigma}_{\sigma\sigma'} c_{i\alpha\sigma'}$  is the local spin operator and  $n_{i\alpha}$  is the local density operator for Ni  $\alpha$  orbital ( $\alpha = 1, 2$ ).  $\langle ij \rangle$  denotes the in-plane and out-of-plane nearest neighbors, and the in-plane and out-of-plane couplings are  $J_{x/y}^\alpha = J_\alpha$  and  $J_z^\alpha = J'_\alpha$ , respectively. By performing the Fourier transformation,  $H_J$  in momentum space reads

$$H_J = \sum_{\eta\alpha\mathbf{k}\mathbf{k}'} V_{\mathbf{k},\mathbf{k}'}^\alpha P_{\eta\alpha}^\dagger(\mathbf{k}) P_{\eta\alpha}(\mathbf{k}') + \sum_{\mathbf{k}\mathbf{k}'} W_{\mathbf{k},\mathbf{k}'}^\alpha B_\alpha^\dagger(\mathbf{k}) B_\alpha(\mathbf{k}'), \quad (4)$$

with the intra-layer pair operator  $P_{\eta\alpha}^\dagger(\mathbf{k}) = c_{\eta\alpha\uparrow}^\dagger(\mathbf{k}) c_{\eta\alpha\downarrow}^\dagger(-\mathbf{k})$  and the inter-layer pair operator  $B_\alpha^\dagger(\mathbf{k}) = c_{t\alpha\uparrow}^\dagger(\mathbf{k}) c_{b\alpha\downarrow}^\dagger(-\mathbf{k}) + c_{b\alpha\uparrow}^\dagger(\mathbf{k}) c_{t\alpha\downarrow}^\dagger(-\mathbf{k})$ . Here  $V_{\mathbf{k},\mathbf{k}'}^\alpha = -\frac{2J_\alpha}{N} \sum_{\pm} (\cos k_x \pm \cos k_y) (\cos k'_x \pm \cos k'_y)$  and  $W_{\mathbf{k},\mathbf{k}'}^\alpha = -\frac{J'_\alpha}{2N}$  and  $N$  being the number of lattice sites. We

investigate the pairing state for both undoped and doped systems and neglect the no-double-occupancy constraint on this t-J model and then perform a mean-field decoupling and solve the self-consistent gap equations (details in SM). According to our calculations, we find that the pairing state has weak dependence on the ratio  $J'_\alpha/J_\alpha$  between the interlayer exchange couplings and intralayer exchange coupling. By choosing  $J'_1/J_1 = 1/5$  and  $J'_2/J_2 = 1/2$  due to strong interlayer coupling in the  $d_{z^2}$  orbitals, the obtained superconducting gaps in different channels as a function of  $J_1$  and  $J_2$  are shown in Fig.4(a). We find that the  $J_2$  generates a dominant extended  $s$ -wave intralayer pairing in the  $d_{z^2}$  orbital. While, the pairing in the  $d_{x^2-y^2}$  orbital is relatively weak. Interestingly, the interlayer pairing in the  $d_{z^2}$  orbital always has the opposite sign compared to the intralayer correspondence. With increasing exchange couplings, the superconducting gaps increase and the corresponding condensation energy grow rapidly as well, as shown in Fig.4(b). By choosing  $J_1 = J_2 = 0.15$  eV, the obtained superconducting gaps are displayed in Fig.4(c). It is apparent that the superconducting gap on the  $\gamma$  pocket dominates over other pockets and an  $s_{\pm}$ -wave pairing can be identified except some quasi nodal features on the  $\beta$  pocket. As the extended  $s$ -wave form factor is negative, the opposite sign between the intralayer and interlayer pairing in the  $d_{z^2}$  orbital can enhance the gap on the  $\gamma$  pocket and thus is favored. Moreover, we study the effect of external doping on the gap size and the obtained gap evolution as a function of doping is depicted in Fig.4(d) with  $J_1 = J_2 = 0.15$  eV. The optimal doping is achieved around the electron doping  $\delta = 0.15$ , where the gap amplitudes reach the maximum. The  $s$ -wave pairing vanishes when the  $\gamma$  pocket is absent around the heavy electron doping  $\delta = 0.4$ . The obtained pairing state and doping dependent gap are qualitatively consistent with our FRG results despite some quantitative difference in gap distribution on Fermi surfaces.

*Discussion.* In our calculations, we have neglected the orthorhombic distortion in the lattice. As the orthorhombic distortion is along the diagonal direction, the induced mixture of  $s$ - and  $d$ -wave pairing between the NN sites is expected to be not strong. The  $s_{\pm}$ -wave pairing is still dominant according to our calculations. In DFT calculations, the  $d_{z^2}$  bands exhibit noticeable dispersion, resulting a square-like pocket at the  $k_z = \pi$  plane. To deal with the 3D feature, we also construct a 3D TB model and perform calculations at different  $k_z$  planes (see SM). We find that the  $s_{\pm}$ -wave is still preserved. Both our FRG and t-J model calculations show that electron doping can enhance  $T_c$ , and this may be consistent with experimental fact that the samples tend to have deficient oxygen. As  $s_{\pm}$ -wave state possesses sign-reversal superconducting gaps in momentum space, neutron scattering and scanning tunneling microscopy measurements are helpful to identify the pairing symmetry [25–27].

*Conclusion.* We study the pairing symmetry of the nickelates under pressure from both weak-coupling and strong-coupling perspective.

*Note added.* During the preparation of this work, we became aware of several independent studies of electronic struc-

ture and pairing instabilities about  $\text{La}_3\text{Ni}_2\text{O}_7$  [28–31]. Our pairing state is consistent with Ref.[29] and the  $T_c$  evolution

with doping is consistent with Ref.[31].

- 
- [1] J. G. Bednorz and K. A. Müller, *Z. Phys. B* **64**, 189.
- [2] Y. Maeno, H. Hashimoto, K. Yoshida, S. Nishizaki, T. Fujita, J. G. Bednorz, and F. Lichtenberg, *Nature* **372**, 532.
- [3] K. Takada, H. Sakurai, E. Takayama-Muromachi, F. Izumi, R. A. Dilanian, and T. Sasaki, *Nature* **422**, 53.
- [4] P. A. Lee, N. Nagaosa, and X.-G. Wen, *Rev. Mod. Phys.* **78**, 17 (2006).
- [5] J. Hu, C. Le, and X. Wu, *Phys. Rev. X* **5**, 041012 (2015).
- [6] B. Keimer, S. A. Kivelson, M. R. Norman, S. Uchida, and J. Zaanen, *Nature* **518**, 179 (2015).
- [7] D. Li, K. Lee, B. Y. Wang, M. Osada, S. Crossley, H. R. Lee, Y. Cui, Y. Hikita, and H. Y. Hwang, *Nature* **572**, 624 (2019).
- [8] M. Osada, B. Y. Wang, K. Lee, D. Li, and H. Y. Hwang, *Phys. Rev. Mater.* **4**, 121801 (2020).
- [9] G. A. Pan, D. Ferenc Segedin, H. LaBollita, Q. Song, E. M. Nica, B. H. Goodge, A. T. Pierce, S. Doyle, S. Novakov, D. Córdoba Carrizales, A. T. N'Diaye, P. Shafer, H. Paik, J. T. Heron, J. A. Mason, A. Yacoby, L. F. Kourkoutis, O. Erten, C. M. Brooks, A. S. Botana, and J. A. Mundy, *Nature Materials* **21**, 160 (2022).
- [10] N. N. Wang, M. W. Yang, Z. Yang, K. Y. Chen, H. Zhang, Q. H. Zhang, Z. H. Zhu, Y. Uwatoko, L. Gu, X. L. Dong, J. P. Sun, K. J. Jin, and J.-G. Cheng, *Nature Communications* **13**, 4367 (2022).
- [11] X. Ding, C. C. Tam, X. Sui, Y. Zhao, M. Xu, J. Choi, H. Leng, J. Zhang, M. Wu, H. Xiao, X. Zu, M. Garcia-Fernandez, S. Agrestini, X. Wu, Q. Wang, P. Gao, S. Li, B. Huang, K.-J. Zhou, and L. Qiao, *Nature* **615**, 50 (2023).
- [12] H. Sakakibara, H. Usui, K. Suzuki, T. Kotani, H. Aoki, and K. Kuroki, *Phys. Rev. Lett.* **125**, 077003 (2020).
- [13] X. Wu, D. Di Sante, T. Schwemmer, W. Hanke, H. Y. Hwang, S. Raghu, and R. Thomale, *Phys. Rev. B* **101**, 060504(R) (2020).
- [14] Y. Nomura and R. Arita, *Reports on Progress in Physics* **85**, 052501 (2022).
- [15] Y. Gu, S. Zhu, X. Wang, J. Hu, and H. Chen, *Communications Physics* **3**, 84 (2020).
- [16] H. Sun, M. Huo, X. Hu, J. Li, Y. Han, L. Tang, Z. Mao, P. Yang, B. Wang, J. Cheng, D.-X. Yao, G.-M. Zhang, and M. Wang, (2023), [arXiv:2305.09586](https://arxiv.org/abs/2305.09586).
- [17] Y. Kamihara, T. Watanabe, M. Hirano, and H. Hosono, **130**, 3296, publisher: American Chemical Society.
- [18] G. R. Stewart, *Rev. Mod. Phys.* **83**, 1589 (2011).
- [19] Z. Luo, X. Hu, M. Wang, W. Wú, and D.-X. Yao, (2023), [arXiv:2305.15564](https://arxiv.org/abs/2305.15564).
- [20] H. Sakakibara, K. Suzuki, H. Usui, S. Miyao, I. Maruyama, K. Kusakabe, R. Arita, H. Aoki, and K. Kuroki, *Phys. Rev. B* **89**, 224505 (2014).
- [21] W. Metzner, M. Salmhofer, C. Honerkamp, V. Meden, and K. Schönhammer, *Rev. Mod. Phys.* **84**, 299 (2012).
- [22] C. Platt, W. Hanke, and R. Thomale, *Advances in Physics* **62**, 453 (2013), <https://doi.org/10.1080/00018732.2013.862020>.
- [23] Q. Si and E. Abrahams, *Phys. Rev. Lett.* **101**, 076401 (2008).
- [24] K. Seo, B. A. Bernevig, and J. Hu, *Phys. Rev. Lett.* **101**, 206404 (2008).
- [25] P. J. Hirschfeld, M. M. Korshunov, and I. I. Mazin, *Reports on Progress in Physics* **74**, 124508 (2011).
- [26] A. D. Christianson, E. A. Goremychkin, R. Osborn, S. Rosenkranz, M. D. Lumsden, C. D. Malliakas, I. S. Todorov, H. Claus, D. Y. Chung, M. G. Kanatzidis, R. I. Bewley, and T. Guidi, *Nature* **456**, 930 (2008).
- [27] T. Hanaguri, S. Niitaka, K. Kuroki, and H. Takagi, *Science* **328**, 474 (2010), <https://www.science.org/doi/pdf/10.1126/science.1187399>.
- [28] Y. Zhang, L.-F. Lin, A. Moreo, and E. Dagotto, (2023), [arXiv:2306.03231](https://arxiv.org/abs/2306.03231).
- [29] Q.-G. Yang, H.-Y. Liu, D. Wang, and Q.-H. Wang, (2023), [arXiv:2306.03706](https://arxiv.org/abs/2306.03706).
- [30] F. Lechermann, J. Gondolf, S. Bötzel, and I. M. Eremin, (2023), [arXiv:2306.05121](https://arxiv.org/abs/2306.05121).
- [31] H. Sakakibara, N. Kitamine, M. Ochi, and K. Kuroki, (2023), [arXiv:2306.06039](https://arxiv.org/abs/2306.06039).
- [32] G. Kresse and J. Furthmüller, *Phys. rev. B* **54**, 11169 (1996).
- [33] G. Kresse and D. Joubert, *Phys. Rev. B* **59**, 1758 (1999).
- [34] J. P. Perdew, K. Burke, and M. Ernzerhof, *Phys. Rev. Lett.* **77**, 3865 (1996).
- [35] A. A. Mostofi, J. R. Yates, Y.-S. Lee, I. Souza, D. Vanderbilt, and N. Marzari, *Comput. Phys. Commun.* **178**, 685 (2008).
- [36] N. Marzari, A. A. Mostofi, J. R. Yates, I. Souza, and D. Vanderbilt, *Rev. Mod. Phys.*, 1419 (2012).
- [37] W. Setyawan and S. Curtarolo, *Computational materials science* **49**, 299 (2010).

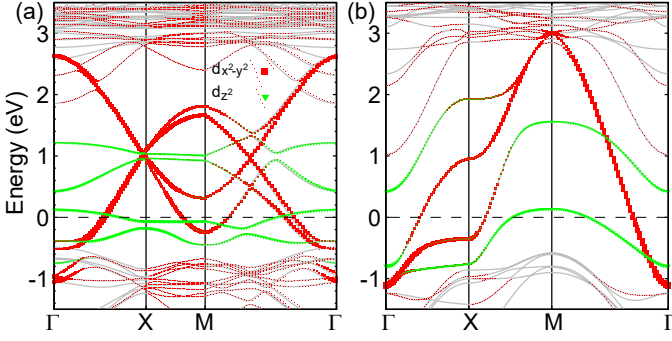


FIG. 5: (color online) The DFT band structures of  $\text{La}_3\text{Ni}_2\text{O}_7$  under (a) ambient pressure and (b) high pressure with primitive cells. The orbital characters near Fermi level are represented by different colors.

### Appendix A: Computational methods

Our electronic structure calculations employ the Vienna ab initio simulation package (VASP) code[32] with the projector augmented wave (PAW) method[33]. The Perdew-Burke-Ernzerhof (PBE)[34] exchange-correlation functional is used in our calculations. The kinetic energy cutoff is set to be 600 eV for the expanding the wave functions into a plane-wave basis and the energy convergence criterion is  $10^{-7}$  eV. We employ the primitive cells of  $\text{La}_3\text{Ni}_2\text{O}_7$  under ambient pressure and high pressure to perform calculations. We optimize the atomic positions until the force is less than 0.005 eV/Å with the experimental lattice constants. The  $\Gamma$ -centered  $\mathbf{k}$ -meshes are  $9 \times 9 \times 9$  and  $14 \times 14 \times 14$  and for ambient pressure phase and high pressure phase, respectively.

We employ Wannier90[35, 36] to calculate maximally localized Wannier functions and the disentangled bands. The initial projectors are Ni's  $d_{x^2-y^2} + d_{z^2}$  orbitals. We fit the effective tight-binding model with the data of the disentangled bands near the Fermi energy.

### Appendix B: electronic structures under ambient pressure and high pressure

High-temperature superconductivity is observed to emerge in the high-pressure phase of  $\text{La}_3\text{Ni}_2\text{O}_7$  rather than in the ambient-pressure phase. To investigate the differences between these phases, Fig.5 show band structures for  $\text{La}_3\text{Ni}_2\text{O}_7$  under both ambient pressure and high pressure, which clearly reveal the presence of the bonding state  $d_{z^2}^+$  band and the anti-bonding state  $d_{z^2}^-$  band. With the application of external pressure,  $\text{La}_3\text{Ni}_2\text{O}_7$  undergoes a structural transition from the *Amam* phase to the more symmetric *Fmmm* phase, which effectively suppresses the octahedral tilting [16]. Consequently, the bands originating from the  $d_{x^2-y^2}$  orbital, the bonding and anti-bonding states  $d_{z^2}^\pm$ , exhibit an increased band width. Additionally, a slight enhancement is observed in the energy splitting between the bonding and anti-bonding state bands.

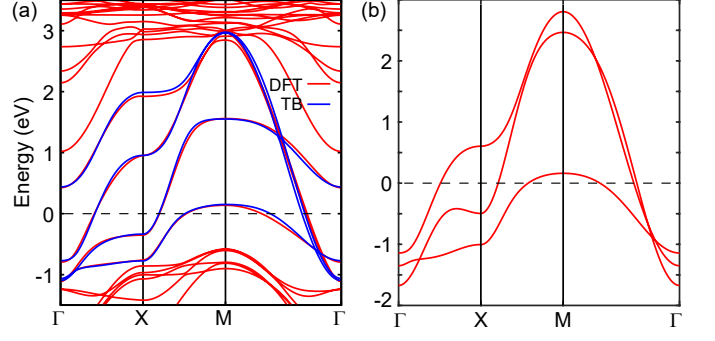


FIG. 6: (color online). (a) The band structures from DFT calculations and four-band effective model. (b) The band structure of three-band effective model.

### Appendix C: bilayer two-orbital model and Three band model on the square lattice

The matrix representation of the bilayer two-band model discussed on the square lattice in the main text can be expressed as follows:

$$h(\mathbf{k}) = \begin{pmatrix} h_{11}(\mathbf{k}) & h_{12}(\mathbf{k}) & h_{13}(\mathbf{k}) & h_{14}(\mathbf{k}) \\ h_{12}^*(\mathbf{k}) & h_{22}(\mathbf{k}) & h_{23}(\mathbf{k}) & h_{24}(\mathbf{k}) \\ h_{13}^*(\mathbf{k}) & h_{23}^*(\mathbf{k}) & h_{33}(\mathbf{k}) & h_{34}(\mathbf{k}) \\ h_{14}^*(\mathbf{k}) & h_{24}^*(\mathbf{k}) & h_{34}^*(\mathbf{k}) & h_{44}(\mathbf{k}) \end{pmatrix}, \quad (\text{C1})$$

where the basis operator is denoted by  $\psi_{\mathbf{k}\sigma}^\dagger = [c_{t_x^2\sigma}^\dagger(\mathbf{k}), c_{t_z^2\sigma}^\dagger(\mathbf{k}), c_{b_x^2\sigma}^\dagger(\mathbf{k}), c_{b_z^2\sigma}^\dagger(\mathbf{k})]$ . The band structures obtained from density functional theory (DFT) calculations and the bilayer two-band model are presented in Fig.6(a), revealing a close agreement near the Fermi level. Then, the matrix elements in the Hamiltonian  $h(\mathbf{k})$  matrix can be given by

$$\begin{aligned} h_{11}(\mathbf{k}) &= h_{33}(\mathbf{k}) = \epsilon_{x^2} + 2t_{11}^x (\cos k_x + \cos k_y) \\ &\quad + 4t_{11}^{xy} \cos k_x \cos k_y + 2t_{11}^{xx} (\cos 2k_x + \cos 2k_y), \\ h_{22}(\mathbf{k}) &= h_{44}(\mathbf{k}) = \epsilon_{z^2} + 2t_{22}^x (\cos k_x + \cos k_y) \\ &\quad + 4t_{22}^{xy} \cos k_x \cos k_y + 2t_{22}^{xx} (\cos 2k_x + \cos 2k_y), \\ h_{12}(\mathbf{k}) &= 2t_{12}^x (\cos k_x - \cos k_y) + 2t_{12}^{xx} (\cos 2k_x - \cos 2k_y), \\ h_{13}(\mathbf{k}) &= s_{11}^0 + 2s_{11}^x (\cos k_x + \cos k_y) + 4s_{11}^{xy} \cos k_x \cos k_y \\ &\quad + 2s_{11}^{xx} (\cos 2k_x + \cos 2k_y), \\ h_{14}(\mathbf{k}) &= 2s_{12}^x (\cos k_x - \cos k_y) + 2s_{12}^{xx} (\cos 2k_x - \cos 2k_y), \\ h_{24}(\mathbf{k}) &= s_{22}^0 + 2s_{22}^x (\cos k_x + \cos k_y) + 4s_{22}^{xy} \cos k_x \cos k_y \\ &\quad + 2s_{22}^{xx} (\cos 2k_x + \cos 2k_y), \\ h_{23}(\mathbf{k}) &= h_{14}(\mathbf{k}), h_{34}(\mathbf{k}) = h_{12}(\mathbf{k}) \end{aligned} \quad (\text{C2})$$

The corresponding tight binding parameters are specified in unit of eV as

$$\begin{aligned}
\epsilon_{x^2} &= 10.929, t_{11}^x = -0.505, t_{11}^{xy} = 0.060, t_{11}^{xx} = -0.047, \\
\epsilon_{z^2} &= 10.474, t_{22}^x = -0.126, t_{22}^{xy} = -0.003, t_{22}^{xx} = -0.021, \\
s_{11}^0 &= -0.049, s_{11}^x = 0.001, s_{11}^{xy} = 0.035, s_{11}^{xx} = -0.022, \\
s_{22}^0 &= -0.628, s_{22}^x = 0.011, s_{22}^{xy} = -0.032, s_{22}^{xx} = 0.024, \\
t_{12}^x &= 0.253, t_{12}^{xx} = 0.037, s_{12}^x = -0.038, s_{12}^{xx} = -0.009. \quad (C3)
\end{aligned}$$

where  $t_{\alpha\beta}^m$  and  $s_{\alpha\beta}^m$  ( $m = 1, 2$ ) represent the intralayer and

$$\begin{aligned}
h'(\mathbf{k}) &= U h(\mathbf{k}) U^{-1} \\
&= \begin{pmatrix} h_{11} & \frac{1}{\sqrt{2}}[h_{12} + h_{14}] & h_{13} & \frac{1}{\sqrt{2}}[h_{12} - h_{14}] \\ \frac{1}{\sqrt{2}}[h_{12}^* + h_{14}^*] & \frac{1}{2}[h_{22} + h_{24} + h_{24}^* + h_{44}] & \frac{1}{\sqrt{2}}[h_{23} + h_{34}^*] & 0 \\ h_{13}^* & \frac{1}{\sqrt{2}}[h_{23}^* + h_{34}] & h_{33} & \frac{1}{\sqrt{2}}[h_{23}^* - h_{34}] \\ \frac{1}{\sqrt{2}}[h_{12}^* - h_{14}^*] & 0 & \frac{1}{\sqrt{2}}[h_{23} - h_{34}^*] & \frac{1}{2}[h_{22} - h_{24} - h_{24}^* + h_{44}] \end{pmatrix}, U = \begin{pmatrix} 1 & 0 & 0 & 0 \\ 0 & \frac{1}{\sqrt{2}} & 0 & \frac{1}{\sqrt{2}} \\ 0 & 0 & 1 & 0 \\ 0 & \frac{1}{\sqrt{2}} & 0 & -\frac{1}{\sqrt{2}} \end{pmatrix} \quad (C4)
\end{aligned}$$

Then, the corresponding basis operator is transformed to  $\psi_{\mathbf{k}\sigma}^\dagger = [c_{tx^2\sigma}^\dagger(\mathbf{k}), c_{+,z^2\sigma}^\dagger(\mathbf{k}), c_{bx^2\sigma}^\dagger(\mathbf{k}), c_{-,z^2\sigma}^\dagger(\mathbf{k})]$  with  $c_{\pm,z^2\sigma}^\dagger(\mathbf{k}) = \frac{1}{\sqrt{2}}(c_{tz^2\sigma}^\dagger(\mathbf{k}) \pm c_{bz^2\sigma}^\dagger(\mathbf{k}))$ . Considering that the band structure associated with the antibonding state  $d_{z^2}^-$  is located away from the Fermi level, it can be neglected, leading to the further simplification of the bilayer two-orbital model into a three-band model. The three-band model can be written as  $\tilde{\mathcal{H}}_{\text{TB}} = \sum_{\mathbf{k}\sigma} \psi_{\mathbf{k}\sigma}^\dagger [\tilde{h}(\mathbf{k}) - \tilde{\mu}] \psi_{\mathbf{k}\sigma}$ , where the matrix elements in the Hamiltonian  $\tilde{h}(\mathbf{k})$  matrix are given by

$$\begin{aligned}
\tilde{h}_{11}(\mathbf{k}) &= \tilde{h}_{33}(\mathbf{k}) = \tilde{\epsilon}_{x^2} + 2\tilde{t}_{11}^x (\cos k_x + \cos k_y) \\
&\quad + 4\tilde{t}_{11}^{xy} \cos k_x \cos k_y + 2\tilde{t}_{11}^{xx} (\cos 2k_x + \cos 2k_y), \\
\tilde{h}_{22}(\mathbf{k}) &= \tilde{\epsilon}_{z^2} + 2\tilde{t}_{22}^x (\cos k_x + \cos k_y) \\
&\quad + 4\tilde{t}_{22}^{xy} \cos k_x \cos k_y + 2\tilde{t}_{22}^{xx} (\cos 2k_x + \cos 2k_y), \\
\tilde{h}_{12}(\mathbf{k}) &= 2\tilde{t}_{12}^x (\cos k_x - \cos k_y) + 2\tilde{t}_{12}^{xx} (\cos 2k_x - \cos 2k_y), \\
\tilde{h}_{13}(\mathbf{k}) &= \tilde{s}_{11}^0 + 2\tilde{s}_{11}^x (\cos k_x + \cos k_y) + 4\tilde{s}_{11}^{xy} \cos k_x \cos k_y \\
&\quad + 2\tilde{s}_{11}^{xx} (\cos 2k_x + \cos 2k_y), \\
\tilde{h}_{23}(\mathbf{k}) &= \tilde{h}_{12}(\mathbf{k}) \quad (C5)
\end{aligned}$$

The corresponding tight binding parameters are specified in unit of eV as

$$\begin{aligned}
\tilde{\epsilon}_{x^2} &= 10.746, \tilde{t}_{11}^x = -0.518, \tilde{t}_{11}^{xy} = 0.097, \tilde{t}_{11}^{xx} = -0.079, \\
\tilde{\epsilon}_{z^2} &= 9.869, \tilde{t}_{22}^x = -0.163, \tilde{t}_{22}^{xy} = -0.004, \tilde{t}_{22}^{xx} = -0.022, \\
\tilde{s}_{11}^0 &= 0.05, \tilde{s}_{11}^x = -0.001, \tilde{s}_{11}^{xy} = -0.014, \tilde{s}_{11}^{xx} = 0.043, \\
\tilde{t}_{12}^x &= 0.134, \tilde{t}_{12}^{xx} = 0.034, \quad (C6)
\end{aligned}$$

Based on the valence of  $\text{Ni}^{2.5+}$ , the electron filling in our model corresponds to  $n = 3$ , with  $\tilde{\mu} = 10.256\text{eV}$ . The band structure is depicted in Fig.6 (b), and it demonstrates good agreement with the results obtained from DFT calculations.

interlayer hopping, respectively. According to the valence of  $\text{Ni}^{2.5+}$ , the electron filling in our model is  $n = 3$  with  $\mu = 10.0585\text{eV}$ . Since the band structures at the fermi level are predominantly attributed to  $d_{x^2-y^2}$  orbital and bonding state  $d_{z^2}^+$ , a unitary transformation can be applied to the aforementioned effective model to provide a more accurate description of the low-energy physics. As a result, the effective model is transformed into the following form:

#### Appendix D: Tight-binding model with $k_z$ dispersion

In order to describe  $k_z$  dispersion, we have to consider inter-bilayer hopping in  $\text{La}_3\text{Ni}_2\text{O}_7$ . If we neglect the orthorhombic distortion of  $Fmmm$  phase  $\text{La}_3\text{Ni}_2\text{O}_7$ , the the basis operator is extended to

$$\begin{aligned}
\psi_{\mathbf{k}\sigma}^\dagger &= [c_{tx^2\sigma}^\dagger(\mathbf{k}), c_{tz^2\sigma}^\dagger(\mathbf{k}), c_{bx^2\sigma}^\dagger(\mathbf{k}), c_{bz^2\sigma}^\dagger(\mathbf{k}), \\
&\quad c_{t'x^2\sigma}^\dagger(\mathbf{k}), c_{t'z^2\sigma}^\dagger(\mathbf{k}), c_{b'x^2\sigma}^\dagger(\mathbf{k}), c_{b'z^2\sigma}^\dagger(\mathbf{k})]. \quad (D1)
\end{aligned} \quad (D2)$$

, as there are four Ni-O layers in one unit cell.

The  $k_z$ -dependent TB model has such form:

$$H_{3D}(\mathbf{k}) = \begin{pmatrix} H_{2D} & H_z \\ H_z^\dagger & H_{2D} \end{pmatrix}, \quad (D3)$$

where  $H_{2D}$  is our four-band effective model in the main text.  $H_z$  includes the hopping between two Ni-O bilayers:

$$H_z(\mathbf{k}) = \begin{pmatrix} H_{11}(\mathbf{k}) & 0 & H_{13}(\mathbf{k}) & 0 \\ 0 & H_{22}(\mathbf{k}) & 0 & H_{24}(\mathbf{k}) \\ H_{13}^*(\mathbf{k}) & 0 & H_{11}(\mathbf{k}) & 0 \\ 0 & H_{24}^*(\mathbf{k}) & 0 & H_{22}(\mathbf{k}) \end{pmatrix}, \quad (D4)$$

whose matrix elements are given by:

$$\begin{aligned}
H_{11}(\mathbf{k}) &= 4s_{11}^z \cos(\frac{k_z}{2}) (\cos(\frac{k_x}{2}) + \cos(\frac{k_y}{2})), \\
H_{22}(\mathbf{k}) &= 4s_{22}^z \cos(\frac{k_z}{2}) (\cos(\frac{k_x}{2}) + \cos(\frac{k_y}{2})), \\
H_{13}(\mathbf{k}) &= 2s_{13}^z e^{i\delta_z k_z} (\cos(\frac{k_x}{2}) + \cos(\frac{k_y}{2})), \\
H_{24}(\mathbf{k}) &= 2s_{24}^z e^{i\delta_z k_z} (\cos(\frac{k_x}{2}) + \cos(\frac{k_y}{2})). \quad (D5)
\end{aligned}$$

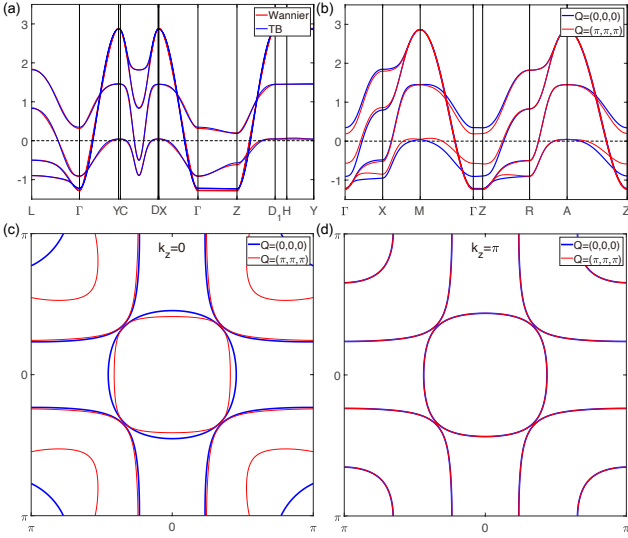


FIG. 7: (color online) (a) The band structures of  $\text{La}_3\text{Ni}_2\text{O}_7$  under high pressure (29.5 GPa) from disentangled Wannierization (red lines) and the  $k_z$ -dependent TB model (blue lines). Noting that the Wannierization result can perfectly reproduce the energy dispersion of the DFT result. The notations of high symmetry  $k$ -points are same as the reference's[37]. (b) The band structure of the block-diagonalized  $k_z$ -dependent TB model. The high symmetry  $k$ -points here are set as in a hypothetical tetragonal unit cell with 4 Ni atoms (neglecting the orthorhombic distortion of the conventional cell of  $\text{La}_3\text{Ni}_2\text{O}_7$  under high pressure). The red lines are the folded energy bands with a folding vector  $\mathbf{Q}=(\pi, \pi, \pi)$ . (c-d) The fermi surfaces of the block-diagonalized  $k_z$ -dependent TB model in (c)  $k_z = 0$  plane and (d)  $k_z = \pi$  plane. The red lines are the folded Fermi surfaces with a folding vector  $\mathbf{Q}=(\pi, \pi, \pi)$ .

The fitted TB parameters are specified in unit of eV as:

$$\begin{aligned} s_{11}^z &= 0.0004, s_{13}^z = 0.0009, \\ s_{22}^z &= -0.0055, s_{24}^z = -0.031. \end{aligned} \quad (\text{D6})$$

As shown in Fig.7(a), our  $k_z$ -dependent TB model can faithfully reproduce our Wannierization result.

We note that we can connect two bilayers with one translational symmetry ( $a/2, a/2, c/2$ ). As a result, we can transfer the  $8 \times 8$   $k_z$ -dependent TB model into a block-diagonalized matrix with using the translational symmetry:

$$H_{3D}^{eff}(\mathbf{k}) = \begin{pmatrix} H_k & 0 \\ 0 & H_{k+Q} \end{pmatrix}, \quad (\text{D7})$$

here  $H_k$  is the effective four-band model and  $Q = (\pi, \pi, \pi)$ . The explicit forms of  $H_k$  and  $H_{k+Q}$  are

$$H_k = \frac{1}{2}(H_{2D} + H_z), H_{k+Q} = \frac{1}{2}(H_{2D} - H_z), \quad (\text{D8})$$

## Appendix E: pairing from the t-J model

In the strong-coupling limit, we adopt the two-orbital t-J model to investigate pairing symmetries for nickelates similar to iron-based superconductors [23, 24] and consider both the in-plane and out-of-plane antiferromagnetic couplings between the spin of Ni  $d_{x^2-y^2}/d_{z^2}$  orbitals,

$$H_J = \sum_{\langle ij \rangle \alpha} J_{ij}^\alpha (\mathbf{S}_{i\alpha} \mathbf{S}_{j\alpha} - \frac{1}{4} n_{i\alpha} n_{j\alpha}) \quad (\text{E1})$$

where  $\mathbf{S}_{i\alpha} = \frac{1}{2} c_{i\alpha\sigma}^\dagger \boldsymbol{\sigma}_{\sigma\sigma'} c_{i\alpha\sigma'}$  is the local spin operator and  $n_{i\alpha}$  is the local density operator for Ni  $\alpha$  orbital ( $\alpha = 1, 2$ ).  $\langle ij \rangle$  denotes the in-plane and out-of-plane nearest neighbors. and the in-plane and out-of-plane couplings are  $J_{x/y}^\alpha = J_\alpha$  and  $J_z^\alpha = J'_\alpha$ , respectively. By performing the Fourier transformation,  $H_J$  in momentum space reads

$$H_J = \sum_{\eta\alpha\mathbf{k}\mathbf{k}'} V_{\mathbf{k},\mathbf{k}'}^\alpha P_{\eta\alpha}^\dagger(\mathbf{k}) P_{\eta\alpha}(\mathbf{k}') + \sum_{\mathbf{k}\mathbf{k}'} W_{\mathbf{k},\mathbf{k}'}^\alpha B_\alpha^\dagger(\mathbf{k}) B_\alpha(\mathbf{k}'), \quad (\text{E2})$$

with the intra-layer pair operator  $P_{\eta\alpha}^\dagger(\mathbf{k}) = c_{\eta\alpha\uparrow}^\dagger(\mathbf{k}) c_{\eta\alpha\downarrow}^\dagger(-\mathbf{k})$  and the inter-layer pair operator  $B_\alpha^\dagger(\mathbf{k}) = c_{t\alpha\uparrow}^\dagger(\mathbf{k}) c_{b\alpha\downarrow}^\dagger(-\mathbf{k}) + c_{b\alpha\uparrow}^\dagger(\mathbf{k}) c_{t\alpha\downarrow}^\dagger(-\mathbf{k})$ . Here  $V_{\mathbf{k},\mathbf{k}'}^\alpha = -\frac{2J_\alpha}{N} \sum_{\pm} (\cos k_x \pm \cos k_y) (\cos k'_x \pm \cos k'_y)$  and  $W_{\mathbf{k},\mathbf{k}'}^\alpha = -\frac{J'_\alpha}{2N}$  and  $N$  being the number of lattice sites. We investigate the pairing state for both undoped and doped systems and neglect the the no-double-occupance constraint on this t-J model and perform a mean-field decoupling. With this, the total Hamiltonian can be written as,

$$\begin{aligned} H_{MF} &= \sum_{\mathbf{k}} \Psi_{\mathbf{k}}^\dagger A(\mathbf{k}) \Psi_{\mathbf{k}} + \frac{N}{2} \sum_{\alpha,\nu=s,d} \frac{|\Delta_\nu^\alpha|^2}{J_\alpha} \\ &+ 2N \sum_{\alpha} \frac{|\Delta_{inter}^\alpha|^2}{J'_\alpha}, \end{aligned} \quad (\text{E3})$$

$$\begin{aligned} A(\mathbf{k}) &= \begin{pmatrix} h(\mathbf{k}) & \Delta_{\uparrow\downarrow}(\mathbf{k}) \\ \Delta_{\uparrow\downarrow}^\dagger(\mathbf{k}) & -h^*(-\mathbf{k}) \end{pmatrix}, \\ \Delta_{\uparrow\downarrow}(\mathbf{k}) &= \begin{pmatrix} \Delta_1^t(\mathbf{k}) & \Delta_2^t(\mathbf{k}) & \Delta_1^{tb} & \Delta_2^{tb} \\ \Delta_1^{bt} & \Delta_2^{bt} & \Delta_1^b(\mathbf{k}) & \Delta_2^b(\mathbf{k}) \end{pmatrix}, \end{aligned} \quad (\text{E4})$$

where  $\Psi_{\mathbf{k}}^\dagger = (\psi_{\mathbf{k}\uparrow}^\dagger, \psi_{-\mathbf{k}\downarrow}^T)$ ,  $\Delta_\alpha^{t/b}(\mathbf{k}) = \Delta_s^{\alpha,t/b} (\cos k_x + \cos k_y) + \Delta_d^{\alpha,t/b} (\cos k_x - \cos k_y)$ ,  $\Delta_\alpha^{tb/bt} = \Delta_{inter}^\alpha$ , and

$$\Delta_{s/d}^{\alpha,\eta} = -\frac{2J_\alpha}{N} \sum_{\mathbf{k}'} d_{\mathbf{k}'\uparrow}^{\alpha,\eta} (\cos k'_x \pm \cos k'_y), \quad (\text{E5})$$

$$\Delta_{inter}^\alpha = -\frac{J'_\alpha}{2N} \sum_{\mathbf{k}'} g_{\mathbf{k}'\uparrow}^\alpha, \quad (\text{E6})$$

with  $d_{\mathbf{k}'\uparrow}^{\alpha,\eta} = \langle c_{\eta\alpha\downarrow}(-\mathbf{k}') c_{\eta\alpha\uparrow}(\mathbf{k}') \rangle$  and  $g_{\mathbf{k}'\uparrow}^\alpha = \langle c_{b\alpha\downarrow}(-\mathbf{k}') c_{t\alpha\uparrow}(\mathbf{k}') + c_{t\alpha\downarrow}(-\mathbf{k}') c_{b\alpha\uparrow}(\mathbf{k}') \rangle$ .  $A(\mathbf{k})$  can be

diagonalized by an unitary transformation  $U_{\mathbf{k}}$  with and the Bogoliubov quasiparticle eigenvalues  $E_{m+4} = -E_m$  with  $m = 1, 2, 3, 4$ . The self-consistent gap equations are

$$\begin{aligned}
\Delta_{s/d}^{1,t/b} &= -\frac{2J_1}{N} \sum_{\mathbf{k},m} (\cos k_x \pm \cos k_y) U_{5/7,m}^*(\mathbf{k}) U_{1/3,m}(\mathbf{k}) F[E_m(\mathbf{k})] \\
\Delta_{s/d}^{2,t/b} &= -\frac{2J_2}{N} \sum_{\mathbf{k},m} (\cos k_x \pm \cos k_y) U_{6/8,m}^*(\mathbf{k}) U_{2/4,m}(\mathbf{k}) F[E_m(\mathbf{k})] \\
\Delta_{inter}^1 &= -\frac{2J'_1}{N} \sum_{\mathbf{k},m} [U_{7,m}^*(\mathbf{k}) U_{1,m}(\mathbf{k}) \\
&\quad + U_{5,m}^*(\mathbf{k}) U_{3,m}(\mathbf{k})] F[E_m(\mathbf{k})] \\
\Delta_{inter}^2 &= -\frac{2J'_2}{N} \sum_{\mathbf{k},m} [U_{8,m}^*(\mathbf{k}) U_{2,m}(\mathbf{k}) \\
&\quad + U_{6,m}^*(\mathbf{k}) U_{4,m}(\mathbf{k})] F[E_m(\mathbf{k})]
\end{aligned} \tag{E7}$$

where  $F[E]$  is Fermi-Dirac distribution function,  $F[E] = 1/(1 + e^{E/k_B T})$ . The above equations can be solved self-consistently, varying the doping and the value of  $J_1, J_2, J'_1, J'_2$ .